AIAA SciTech Forum
6-10 January 2020, Orlando, FL
AIAA Scitech 2020 Forum

10.2514/6.2020-2062

Wall-resolved implicit large eddy simulation of transonic buffet over the OAT15A airfoil using a discontinuous Galerkin method

Ngoc-Cuong Nguyen*, Sebastien Terrana†, and Jaime Peraire‡
Department of Aeronautics and Astronautics, Massachusetts Institute of Technology, Cambridge, MA, 02139

We present a wall-resolved implicit large eddy simulation (WRILES) of transonic buffet over the OAT15A supercritical airfoil at at Mach number 0.73, angle of attack 3.5^o and Reynolds number 3×10^6. The simulation is performed using a high-order discontinuous Galerkin (DG) method and a diagonally implicit Runge-Kutta (DIRK) scheme on graphics processor units (GPUs). In order to effectively resolve the boundary layers at high Reynolds numbers, we develop a LES mesh refinement strategy to provide adequate resolution in the normal and streamwise/crossflow directions while keeping the aspect ratio of the elements below 20. Without yhe need for subgrid scale or wall models, the WRILES method successfully predicts the buffet onset, the buffet frequency, and turbulence statistics. Various turbulence phenomena are predicted and demonstrated, such as periodical low-frequency oscillations of shock wave in the streamwise direction, strong shear layer detached from the shock wave due to shock wave boundary layer interaction (SWBLI) and small scale structures broken down by the shear layer instability in the transition region, and shock-induced flow separation. The pressure coefficient, the root mean square (RMS) of fluctuating pressure and streamwise range of shock wave oscillation agree well with experimental data. The results demonstrate the capability of the WRILES method for predicting the buffet phenomena at high Reynolds numbers.

I. Introduction

Transonic flows over an airfoil result in complex interactions between shock waves and viscous boundary layers. A particularly interesting phenomenon is *transonic buffet*, whereby the flow separation induces a large-scale self-sustained motion of the shock over the surface of the airfoil. Transonic buffet can cause large-scale lift oscillations and structural vibrations that can limit an aircraft's flight envelope. The transonic buffet over the OAT15A airfoil was investigated in the experimental work by Jacquin et al. [1] at a freestream Mach number 0.73 and a chord-based Reynolds number 3×10^6. The OAT15A is a supercritical wing section with a thickness-to-chord ratio of 12.3%, a chord of 0.23 m, and a blunt trailing edge measuring 0.005c. The airfoil model was tripped on both sides at $x/c = 0.07$ from the leading edge. The experiment showed that a periodic self-sustained shock-wave motion was obtained at an angle of attack of 3.5^o with the frequency 69 Hz. The flow dynamics can be summarized as follows: when the shock is at its most upstream position, the boundary layer is separated from the foot of the shock to the trailing edge. As the shock starts moving downstream, the flow reattaches. When the shock reaches its most downstream position, the boundary layer undergoes a progressive thickening until it separates again and the shock starts moving back upstream [2].

The prediction of transonic buffet is challenging due to the co-existence of multiple physical phenomena such as turbulent structures in the thin turbulent boundary layer (TBL) at high Reynolds number, unsteady shock wave, shock-induced separation, acoustic wave generation and propagation, and structural vibrations. In the numerical simulations of transonic buffet using URANS, turbulence models have an immense influence on the the prediction accuracy of the buffet onset. The study of Thiery and Coustols [3] for instance, showed that the BSL and SA models yielded a steady solution, while the KKL and SST models produced periodic shock oscillations. Detached-eddy simulation (DES) is a hybrid approach to simulate turbulent flows by modeling the attached boundary layer with RANS, while resolving the unsteady separated flow with LES. Several studies of transonic buffet over the OAT15A airfoil have been performed by using the various versions of DES [2, 4, 5]. Deck [4] performed both standard DES and zonal DES

*Principal Research Scientist, Department of Aeronautics and Astronautics, Massachusetts Institute of Technology, Cambridge, MA, 02139. Email: cuongng@mit.edu. Senior AIAA member.

†Postdoctoral Associate, Department of Aeronautics and Astronautics, Massachusetts Institute of Technology, Cambridge, MA, 02139. Email: terrana@mit.edu.

‡Professor, Department of Aeronautics and Astronautics, Massachusetts Institute of Technology, Cambridge, MA, 02139. Email: peraire@mit.edu. AIAA Fellow.

(ZDES) of the transonic buffet over the OAT15A airfoil. In that study, ZDES predicted the self-sustained motion of the shock wave and overestimated the size of the shock-induced separation, while standard DES did not reproduce the shock motion. Grossi et al. [2] performed delayed DES (DDES) over the OAT15A airfoil and compared the results with URANS and ZDES. Huang et al. [5] performed the improved DDES (IDDES) with appropriate blending between DDES and wall-modeled LES functionality. However, the sensitivity of the prediction accuracy on the switching location between RANS and LES is a major drawback of the DES approach.

Wall-modeled LES (WMLES) is another turbulence simulation approach in which LES is deployed from the outer part of the boundary layer onward while the unresolved turbulence in the inner part of the boundary layer is modeled. Because LES resolves the turbulence structures all the way down to the outer part of the boundary layer, WMLES is much more computationally expensive than DES. The recent work of Fukushima and Kawai [6] is the first WMLES prediction of the transonic buffet over the OAT15A airfoil. In that work, a subgrid-scale model is used to compute the turbulent eddy viscosity in the LES-resolved region, and the unresolved inner layer is modeled by solving two coupled ordinary differential equations (ODEs) for the wall-parallel velocity and the temperature. A sixth-order compact difference scheme is used for spatial discretization, while a third-order Runge–Kutta scheme is used for time integration. The number of total grid points is about 440 million grid points, which is more or less two orders of magnitude higher than the above-mentioned DES simulations. The minimum grid resolution of the first grid point off the wall is $y^+ \approx 10$ in viscous wall units. This allows a time-step size which is one order of magnitude larger than that of a wall-resolved LES (WRLES) approach. The result obtained by the WMLES shows good agreement with the experiments and turbulence structures are better resolved than those of ZDES, DDES, and IDDES simulations. When LES is used in the entire domain all the way to the wall, the approach is called wall-resolved LES (WRLES). Because WRLES resolves the inner part of the boundary layer, higher-fidelity prediction is possible with WRLES. Garnier and Deck [7] conducted the first WRLES prediction of the transonic buffet over the OAT15A airfoil. In order to limit the required computational effort, the flow is computed in 2D RANS mode on the pressure side of the airfoil and in LES mode on the suction side and in the wake. Despite the zonal treatment of the flow, 20.8 millions of cells are used in their coraser grid, and twice as many are used in their finer grid. The WRLES predictions agree reasonably well with the experiments in terms of the mean field analysis and spectral analysis.

In the classical (explicit) LES approach, the large-scale eddies of the flow field are resolved and the small scales are modeled using an appropriate SGS model. A natural alternative to the SGS-based LES approach is to use the numerical dissipation of the discretization scheme to account for the dissipation that takes place in the unresolved scales, leading to implicit LES (ILES). ILES benefits from its easy implementation without a SGS model and currently gains considerable attention from researchers in the computational fluid dynamics community [8]. As pointed out by Spalart [9], this increase in popularity may be attributed to the fact that research has failed to show an advantage of sophisticated SGS models over the same-cost LES with a simplistic model or even with no model and a slightly finer grid.

Over the past few years, discontinuous Galerkin (DG) methods have emerged as a promising approach for fluid flow simulations. First, they allow for high-order discretizations on complex geometries and unstructured meshes; which is a critical feature to simulate transitional and turbulent flows over the complex three-dimensional geometries commonly encountered in industrial applications. Second, DG methods are well suited to emerging computing architectures, including graphics processing units (GPUs) and other many-core architectures, due to their high flop-to-communication ratio. The use of DG methods for implicit large-eddy simulation of transitional and turbulent flows is being further encouraged by successful numerical predictions [8, 10–16]. Recently, Pazner et al. [17] apply a high-order DG method to the WRLES simulation of transonic buffet on the OAT15A airfoil to study the effect of mesh refinement, polynomial degree, and artificial viscosity parameters.

In this paper, we develop a matrix-free DG method for the wall-resolved implicit large eddy simulation of transonic buffet over the OAT15A supercritical airfoil at at Mach number 0.73, angle of attack 3.5^o and Reynolds number 3×10^6. The paper is organized as follows. In Section 2, we describe the numerical methodology to discretize the governing equations. In Section 3, we discuss and compare the obtained results with the experimental data [1], and with the available numerical experiments: ZDES [4], DDES [2], IDDES [5], and WMLES [6]. Finally, some concluding remarks and a rationale for the success of WRILES for transonic buffet prediction are presented in Section 4.

II. Numerical Methodology

A. Governing equations

Let $t_f > 0$ be a final time and let $\Omega \subset \mathbb{R}^d$, $1 \leq d \leq 3$ be an open, connected and bounded physical domain with Lipschitz boundary $\partial\Omega$. The unsteady compressible Navier-Stokes equations in conservation form are given by

$$\boldsymbol{q} - \nabla \boldsymbol{u} = 0\,, \qquad \text{in } \Omega \times [0, t_f)\,, \tag{1a}$$

$$\frac{\partial \boldsymbol{u}}{\partial t} + \nabla \cdot \boldsymbol{F}(\boldsymbol{u}) + \nabla \cdot \boldsymbol{G}(\boldsymbol{u}, \boldsymbol{q}) = 0\,, \qquad \text{in } \Omega \times [0, t_f)\,, \tag{1b}$$

$$\boldsymbol{B}(\boldsymbol{u}, \boldsymbol{q}) = 0\,, \qquad \text{on } \partial\Omega \times [0, t_f)\,, \tag{1c}$$

$$\boldsymbol{u} - \boldsymbol{u}_0 = 0\,, \qquad \text{on } \Omega \times \{0\}\,. \tag{1d}$$

Here, $\boldsymbol{u} = (\rho, \rho v_j, \rho E),\ j = 1, ..., d$ is the m-dimensional ($m = d + 2$) vector of conserved quantities, $\boldsymbol{u}_0$ is an initial state, $\boldsymbol{B}(\boldsymbol{u}, \boldsymbol{q})$ is a boundary operator, and $\boldsymbol{F}(\boldsymbol{u})$ and $\boldsymbol{G}(\boldsymbol{u}, \boldsymbol{q})$ are the inviscid and viscous fluxes of dimensions $m \times d$,

$$\boldsymbol{F}(\boldsymbol{u}) = \begin{pmatrix} \rho v_j \\ \rho v_i v_j + \delta_{ij} p \\ v_j(\rho E + p) \end{pmatrix}, \qquad \boldsymbol{G}(\boldsymbol{u}, \boldsymbol{q}) = -\begin{pmatrix} 0 \\ \tau_{ij} \\ v_i \tau_{ij} - f_j \end{pmatrix}, \qquad i, j = 1, \ldots, d\,, \tag{2}$$

where p denotes the thermodynamic pressure, τ_{ij} the viscous stress tensor, f_j the heat flux, and δ_{ij} is the Kronecker delta. For a calorically perfect gas in thermodynamic equilibrium, $p = (\gamma - 1)\left(\rho E - \rho \|\boldsymbol{v}\|^2/2\right)$, where $\gamma = c_p/c_v > 1$ is the ratio of specific heats and in particular $\gamma \approx 1.4$ for air. c_p and c_v are the specific heats at constant pressure and volume, respectively. For a Newtonian fluid with the Fourier's law of heat conduction, the viscous stress tensor and heat flux are given by

$$\tau_{ij} = \mu\left(\frac{\partial v_i}{\partial x_j} + \frac{\partial v_j}{\partial x_i} - \frac{2}{3}\frac{\partial v_k}{\partial x_k}\delta_{ij}\right) + \beta\,\frac{\partial v_k}{\partial x_k}\delta_{ij}, \qquad\qquad f_j = -\,\kappa\,\frac{\partial T}{\partial x_j}, \tag{3}$$

where T denotes temperature, μ the dynamic (shear) viscosity, β the bulk viscosity, $\kappa = c_p\,\mu/Pr$ the thermal conductivity, and Pr the Prandtl number. In particular, $Pr \approx 0.71$ for air, and additionally $\beta = 0$ under the Stokes' hypothesis.

B. Shock capturing

To deal with shocks, we extend the physics-based artificial viscosity approach introduced by Fernandez et al. [18]. This approach relies on shock, thermal gradient and shear sensors. The *shock sensor* is constructed such that

$$s_\beta(\mathbf{x}) = s_\theta \cdot s_{\boldsymbol{\omega}}, \qquad s_\theta = -\frac{h_\beta}{k}\frac{\nabla \cdot \mathbf{u}}{a^*}, \qquad s_{\boldsymbol{\omega}} = \frac{(\nabla \cdot \mathbf{u})^2}{(\nabla \cdot \mathbf{u})^2 + |\nabla \times \mathbf{u}|^2 + \varepsilon}, \tag{4}$$

where ε is a constant of the order of the machine precision squared, k is the polynomial degree and a^* is the critical speed of speed of sound. The element size is taken along the direction of the density gradient

$$h_\beta(\mathbf{x}) = h_{\text{ref}}\frac{|\nabla\rho|}{\sqrt{\nabla\rho^T \cdot \mathbf{M}_h^{-1}\nabla\rho + \varepsilon}} \tag{5}$$

where $\mathbf{M}_h$ is the metric tensor of the mesh, and h_{ref} is the size of the reference element used in the construction of $\boldsymbol{M}_h$. The *shear sensor* is also designed to detect under-resolved features, namely velocity gradients, and is constructed from

$$s_\mu(\mathbf{x}) = \frac{h_{\text{ref}}}{k}\frac{\|\boldsymbol{\mathcal{L}}(\mathbf{u}) \cdot \mathbf{x}_{\boldsymbol{\xi}}^T\|_2}{u_{\max}} \tag{6}$$

where $\|\cdot\|_2$ denotes the Euclidean norm, $u_{\max}$ is the maximum isentropic velocity (obtained by reversibly converting all the energy into kinetic energy)

$$u_{\max} = \sqrt{|\mathbf{u}|^2 + \frac{2}{\gamma - 1}a^2}, \qquad \boldsymbol{\mathcal{L}}(\mathbf{u}) = \frac{\partial \mathbf{u}_i}{\partial \mathbf{x}_j}\left(1 - \delta_{ij}\right), \tag{7}$$

with δ_{ij} representing Kronecker's delta.

We then add artificial bulk viscosity and artificial molecular viscosity (β^*, μ^*) to the physical values such that:

$$\beta = \beta_f + \beta^*, \qquad \mu = \mu_f + \mu^*,$$

where the amount of viscosities are determined to ensure a cell Péclet number of $O(1)$ as follows

$$\beta^*(\mathbf{x}) = \hat{s}_\beta \rho \frac{k_\beta h_\beta}{k} \sqrt{|\mathbf{u}|^2 + a^{*2}} \tag{8a}$$

$$\mu^*(\mathbf{x}) = \hat{s}_\mu \rho \frac{k_\mu h_\mu}{k} \sqrt{|\mathbf{u}|^2 + a^{*2}}. \tag{8b}$$

Here $k_{\mu,\kappa} = 1$, $k_\beta = 1.5$, and $\left(\hat{s}_\beta, \hat{s}_\mu\right)$ denote the smoothly bounded values of the sensors in equations (4) and (6). We also note that

$$h_\mu(\mathbf{x}) = h_{\text{ref}} \inf_{|\mathbf{a}|=1} \left\{ \mathbf{a}^T \cdot \mathbf{M}_h \, \mathbf{a} \right\}. \tag{9a}$$

Finally, a smoothing operator is applied to (β^*, μ^*) to make them C^0 continuous. Since at most moderately high accuracy orders are used for the numerical examples in this paper, we employ an element-wise linear reconstruction procedure analogous to that introduced in [19] for the element size.

C. Discontinuous Galerkin method

The DG discretization of the unsteady compressible Navier-Stokes equations reads as follows: Find $\left(\boldsymbol{q}_h(t), \boldsymbol{u}_h(t)\right) \in \boldsymbol{Q}_h^k \times \boldsymbol{\mathcal{V}}_h^k$ such that

$$\left(\boldsymbol{q}_h, \boldsymbol{r}\right)_{\mathcal{T}_h} + \left(\boldsymbol{u}_h, \nabla \cdot \boldsymbol{r}\right)_{\mathcal{T}_h} - \left\langle \widehat{\boldsymbol{u}}_h, \boldsymbol{r} \cdot \boldsymbol{n} \right\rangle_{\partial\mathcal{T}_h} = 0\,, \tag{10a}$$

$$\left(\frac{\partial \boldsymbol{u}_h}{\partial t}, \boldsymbol{w}\right)_{\mathcal{T}_h} - \left(\boldsymbol{F}(\boldsymbol{u}_h) + \boldsymbol{G}(\boldsymbol{u}_h, \boldsymbol{q}_h), \nabla \boldsymbol{w}\right)_{\mathcal{T}_h} + \left\langle \widehat{\boldsymbol{f}}_h(\widehat{\boldsymbol{u}}_h, \boldsymbol{u}_h) + \widehat{\boldsymbol{g}}_h(\widehat{\boldsymbol{u}}_h, \boldsymbol{u}_h, \boldsymbol{q}_h), \boldsymbol{w} \right\rangle_{\partial\mathcal{T}_h} = 0\,, \tag{10b}$$

for all $(\boldsymbol{r}, \boldsymbol{w}, \boldsymbol{\mu}) \in \boldsymbol{Q}_h^k \times \boldsymbol{\mathcal{V}}_h^k \times \boldsymbol{\mathcal{M}}_h^k$ and all $t \in [0, t_f)$, as well as

$$\left(\boldsymbol{u}_h|_{t=0} - \boldsymbol{u}_0, \boldsymbol{w}\right)_{\mathcal{T}_h} = 0\,, \tag{10c}$$

for all $\boldsymbol{w} \in \boldsymbol{\mathcal{V}}_h^k$. The finite element spaces and inner products above are described in [8]. Here $\widehat{\boldsymbol{f}}_h$ and $\widehat{\boldsymbol{g}}_h$ are the inviscid and viscous numerical fluxes which are defined on the interior faces as

$$\widehat{\boldsymbol{f}}_h(\widehat{\boldsymbol{u}}_h, \boldsymbol{u}_h) = \boldsymbol{F}(\widehat{\boldsymbol{u}}_h) \cdot \boldsymbol{n} + \boldsymbol{\sigma}(\widehat{\boldsymbol{u}}_h, \boldsymbol{u}_h; \boldsymbol{n}) \cdot (\boldsymbol{u}_h - \widehat{\boldsymbol{u}}_h)\,, \tag{11a}$$

$$\widehat{\boldsymbol{g}}_h(\widehat{\boldsymbol{u}}_h, \boldsymbol{u}_h, \boldsymbol{q}_h) = \boldsymbol{G}(\widehat{\boldsymbol{u}}_h, \boldsymbol{q}_h) \cdot \boldsymbol{n}\,, \tag{11b}$$

and $\boldsymbol{n}$ is the unit normal vector pointing outwards from the elements. Note that this form of the numerical flux does not involve an explicit Riemann solver. Instead, it is the so-called stabilization matrix $\boldsymbol{\sigma}(\widehat{\boldsymbol{u}}_h, \boldsymbol{u}_h; \boldsymbol{n}) \in \mathbb{R}^{m \times m}$ that implicitly defines the Riemann solver in DG methods. In this paper, we set $\boldsymbol{\sigma} = \lambda_{max}(\widehat{\boldsymbol{u}}_h)\, \boldsymbol{I}_m$, where λ_{max} denotes the maximum-magnitude eigenvalue of $\boldsymbol{A}_n = [\partial \boldsymbol{F} / \partial \boldsymbol{u}] \cdot \boldsymbol{n}$ and $\boldsymbol{I}_m$ is the $m \times m$ identity matrix, and which leads to a Lax-Friedrichs-type Riemann solver. Additional details on this stabilization matrix and the resulting Riemann solver are presented in [8, 20].

It remains to define the numerical trace. Different choices of the numerical trace yield different DG methods. For the local DG (LDG) method [21] the numerical trace is defined as $\widehat{\boldsymbol{u}}_h = \frac{1}{2}(\boldsymbol{u}_h^+ + \boldsymbol{u}_h^-) + (\boldsymbol{u}_h^+ \boldsymbol{\beta} \cdot \boldsymbol{n}^+ + \boldsymbol{u}_h^- \boldsymbol{\beta} \cdot \boldsymbol{n}^-)$ on the interior faces, where $\boldsymbol{\beta}$ is a vector-valued function. Note that $\boldsymbol{u}_h^+ = \boldsymbol{u}_h|_{F \in K^+}$ and $\boldsymbol{u}_h^- = \boldsymbol{u}_h|_{F \in K^-}$ denote the restriction of the numerical solution $\boldsymbol{u}_h$ on interior face F shared by elements K^+ and K^-. On the boundary faces, the definition of the numerical trace depends on the boundary conditions. The hybridized DG (HDG) method [8, 20] does not define the numerical trace $\widehat{\boldsymbol{u}}_h$ terms of the numerical solution. In the HDG method, the numerical trace becomes an additional variable to be solved by introducing another equation that imposes the continuity of the numerical flux $\widehat{\boldsymbol{f}}_h(\widehat{\boldsymbol{u}}_h, \boldsymbol{u}_h) + \widehat{\boldsymbol{g}}_h(\widehat{\boldsymbol{u}}_h, \boldsymbol{u}_h, \boldsymbol{q}_h)$ and enforces boundary conditions. In this paper, the LDG method is used to solve the compressible Navier-Stokes equations since it is suited to a matrix-free iterative solver discussed in the next section.

Finally, the semi-discrete system (10) is further discretized in time using high-order, L-stable diagonally implicit Runge-Kutta (DIRK) schemes [22]. The use of high-order, L-stable methods for the temporal discretization is important for accuracy and robustness when dealing with turbulent shock flows. Also, the use of implicit time integration schemes allows to examine the impact of the shock capturing method on the conditioning of the spatial discretization (10) through the ease of solving the nonlinear system of equations arising from the time discretization.

D. Solution method

The Newton's method is used to solve the nonlinear system of equations resulting from the temporal discretization of the system (10). In order to reduce the number of Newton iterations, we compute the initial guess $\boldsymbol{u}_h^{n,0}$ at n^{th} timestep by solving the following least-squares problem [8]:

$$\boldsymbol{u}_h^{n,0} := \sum_{j=1}^{J} \alpha_j \, \boldsymbol{u}_h^{n-j}$$

where $\boldsymbol{u}_h^l$ denotes the solution at the l^{th} timestep, and

$$(\alpha_1, \ldots, \alpha_J) = \arg \min_{(\beta_1,\ldots,\beta_J)\in\mathbb{R}^J} \left\| \boldsymbol{R}_{\text{NS}}\left(\sum_{j=1}^{J} \beta_j \, \boldsymbol{u}_h^{n-j} \right) \right\| . \tag{12}$$

This optimization problem is solved by using the Levenberg–Marquardt (LM) algorithm [23], where the gradient vectors $\partial \boldsymbol{R}_{\text{NS}}/\partial \beta_j$ are approximated by finite differences. This advanced initialization adds very little to the overall computational cost while reducing the number of Newton iterations compared to the standard initialization using just the previous solution.

In each Newton iteration, we use GMRES to solve the resulting linear system. In order to accelerate the convergence rate of GMRES we develop a matrix-free scalable preconditioner. We briefly describe one of our approaches to preconditioning that will scale linearly with the problem size. The key idea in devising a matrix-free preconditioner lies in the construction of an approximation to the Jacobian matrix $\boldsymbol{J}(\boldsymbol{u}_n)$ of dimension $N \times N$ through a suitable low-rank approximation. Given the mass matrix $\boldsymbol{M}$ and a low-rank matrix $\boldsymbol{W}_n$ of dimension $N \times m$ with $m \ll N$ consisting of the previous solution vectors, our preconditioner has the following form:

$$\boldsymbol{P}_n = \boldsymbol{M} + \boldsymbol{V}_n \boldsymbol{D}_n^{-1} \boldsymbol{W}_n \, , \tag{13}$$

where $\boldsymbol{V}_n$ and $\boldsymbol{D}_n$ are chosen to satisfy the following approximation property:

$$\boldsymbol{P}_n \boldsymbol{W}_n = \boldsymbol{J}(\boldsymbol{u}_n) \boldsymbol{W}_n \, . \tag{14}$$

In order to satisfy this equation, we choose $\boldsymbol{D}_n = \boldsymbol{W}_n^T \boldsymbol{W}_n$ and $\boldsymbol{V}_n = \boldsymbol{J}(\boldsymbol{u}_n)\boldsymbol{W}_n - \boldsymbol{M}\boldsymbol{W}_n$. Using the Sherman–Morrison–Woodbury formula, we compute the inverse of the preconditioner $\boldsymbol{P}_n$ as:

$$\boldsymbol{P}_n^{-1} = \boldsymbol{M}^{-1} - \boldsymbol{M}^{-1} \boldsymbol{V}_n \left(\boldsymbol{D}_n + \boldsymbol{W}_n^T \boldsymbol{M}^{-1} \boldsymbol{V}_n \right)^{-1} \boldsymbol{W}_n^T \boldsymbol{M}^{-1} \, , \tag{15}$$

The low-rank preconditioner of the form (13) can be viewed as a generalization of the BFGS update [24–27] with a distinctive feature that our approach allows for arbitrary-rank approximation, whereas the BFGS update is only a rank-two approximation of the Jacobian matrix.

The computation of $\boldsymbol{J}(\boldsymbol{u}_n)\boldsymbol{W}_n$ can be expensive if we have to form the Jacobian matrix $\boldsymbol{J}(\boldsymbol{u}_n)$ and perform matrix-matrix multiplication. Instead, the product of the Jacobian matrix with any vector $\boldsymbol{y}$ can be approximately computed by the Taylor expansion as follows

$$\boldsymbol{J}(\boldsymbol{u}_n)\, \boldsymbol{y} \approx \frac{\boldsymbol{R}_{\text{NS}}(\boldsymbol{u}_n + \epsilon \boldsymbol{y}) - \boldsymbol{R}_{\text{NS}}(\boldsymbol{y})}{\epsilon} \, , \tag{16}$$

for small enough ϵ. Furthermore, since we only need to compute the first column of the matrix $\boldsymbol{J}(\boldsymbol{u}_n)\boldsymbol{W}_n$, it allows us to construct the preconditioner with only *one evaluation* of the residual vector. With this reduced preconditioning technique, the construction of the preconditioner adds very little cost to the preconditioned accelerated first-order methods described earlier. Therefore the computational complexity of our preconditioned GMRES is comparable to that without preconditioning.

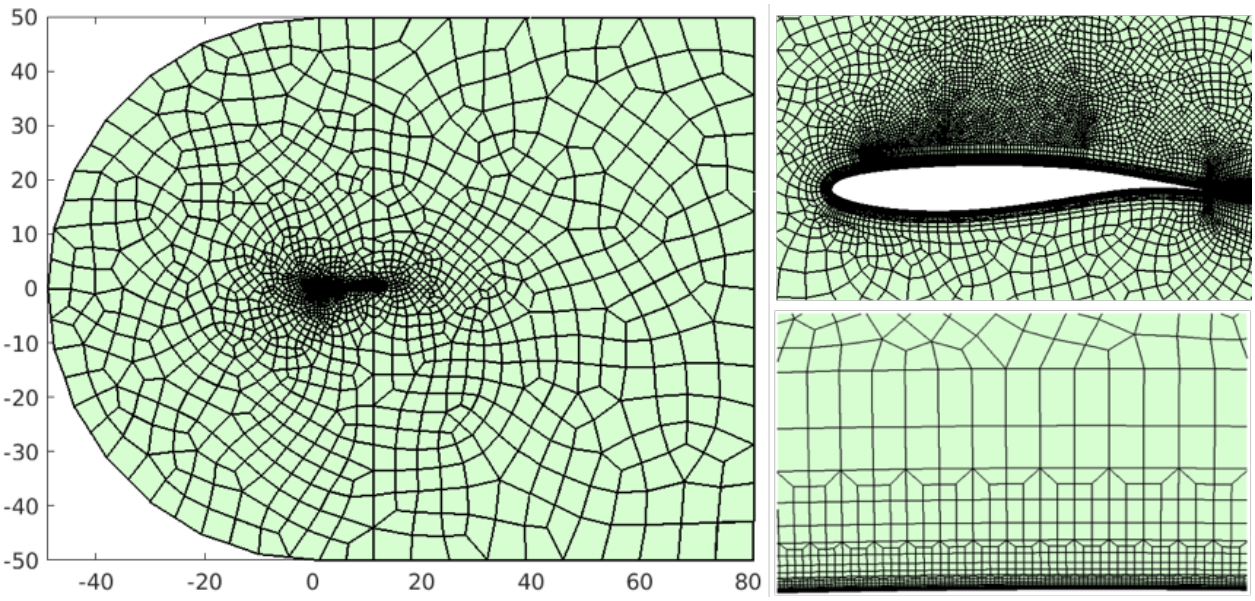

Fig. 1 Section of the mesh used for the present paper. The mesh comprises an unstructured part far from the boundary layer (left), and a more structured part to mesh the boundary layer (right).

E. CUDA/MPI implementation

The proposed discretization schemes and solution methods are implemented in the CUDA-accelerated multiphysics simulations (CAMPS) code, which is written using the C++ programming language with MPI-based parallelization and CUDA for GPUs. Because computing the residual vector is the most expensive operation in all simulations, it must be optimized. The residual vector is computed using Gauss quadrature which involves matrix-matrix multiplication of the form $\boldsymbol{R}_{\mathrm{NS}}(\boldsymbol{u}_n) = \boldsymbol{S} \times \boldsymbol{G}(\boldsymbol{u}_n)$, where $\boldsymbol{S}$ is a small matrix (related to the shape functions and their derivatives at the quadrature points on the master element) and $G(\boldsymbol{u}_n)$ is a very wide matrix. We optimize the residual calculation on GPUs by implementing a number of different algorithms to compute this matrix-matrix multiplication. In particular, tensor-product with sum-factorization is one of the implemented algorithms, while other algorithms involve the customized allocation of GPU's shared memory depending on the size of the matrix S. We use automatic tuning to pick the fastest algorithm depending on the problem dimension, the polynomial degree, the element type, and the particular GPUs. For parallel simulations, we divide the computational domain into subdomains and each GPU is responsible for computing the part of the residual vector on its own subdomain. MPI communication across neighboring subdomains is overlapped with the computation of the residual on the interior elements of each subdomain.

III. Results and Discussions

The mesh used for this study is made of 1.12 million quadratic hexahedra elements, i.e. a total of approximately 30 millions nodes. The final mesh is a 2D mesh extruded over $0.065c$ in the z-direction, and extends over $50c$ around the airfoil in the $(0, x, y)$ plane, see Fig. 1. Also, the mesh geometry takes into account the transition strips as shown in Fig. 2. The strips are located at 7% of the chord length and 3mm wide in the chord direction. On the lower surface, the strip thickness is 0.089mm. On the upper surface, the strip thickness is 0.102mm. These information were obtained from private communication with the authors of the experiment paper [1].

The numerical study is performed with a non-dimensional time step $\Delta t = 10^{-4} c/u_\infty$, and for a total of 95 chord-based time units tu_∞/c. Starting from an extruded 2D solution, the shock oscillations start after $tu_\infty/c \approx 20$. Discarding the initial transient flow, we can record up to 5 full periodic oscillations of the shock, which are used to perform the statistical data presented below. Note that one periodic shock oscillation is defined as the time period in which the shock wave moves from the most upstream position to the downstream and reaches the most upstream position again. One periodic shock oscillation takes about 15 chord-based time units. The whole computation was performed using 32 NVIDIA V100 GPUs at the Barcelona Supercomputer Center for approximately 700 run-time hours.

The pressure coefficients C_p displayed on Fig. 3 are spanwise-averaged and time-averaged over the 5 oscillations

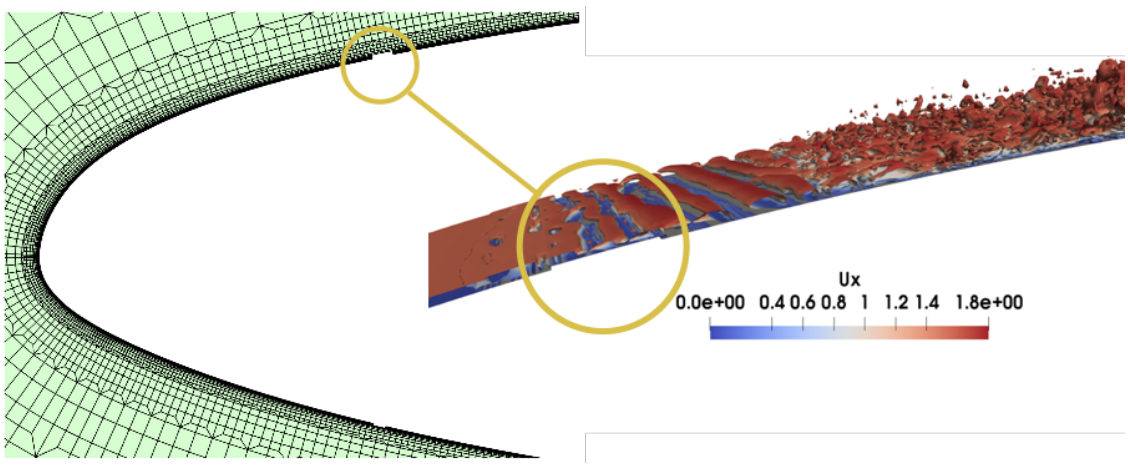

Fig. 2 Zoom of the mesh near the transition strips.

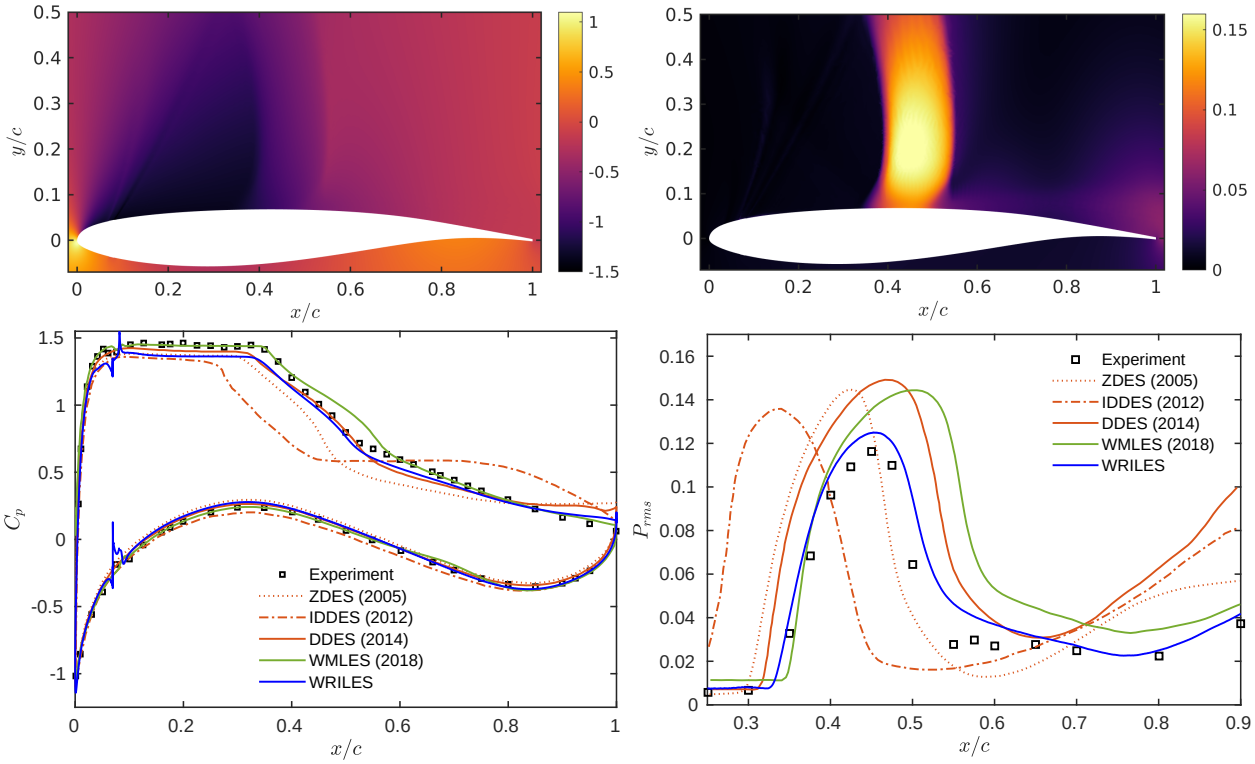

Fig. 3 Left: Comparisons of the spanwise-and-time-averaged pressure coefficients C_p on the airfoil surface. Right: Comparisons of the standard deviations of the pressure P_{rms} on the suction surface.

cycles. The pressure standard deviations P_{rms} are also spanwise-averaged. Comparisons are made with experimental data [1], as well as numerical other numerical simulations (ZDES [4], DDES [2], IDDES [5], and WMLES [6]). The computed C_p agrees very well with the experimental data. The sharp oscillations at $x/c \approx 0.07$ are due to the strip location. The average location of the shock is precisely captured, as well as the averaged pressure in the TBL (see Fig. 3). Behind the shock wave ($x/c \geq 0.6$), the agreement is also fairly good, suggesting that the turbulent reattachment behind the shock wave is correctly predicted by WRILES.

Both the DDES and the WMLES can also predict a fairly accurate distribution of C_p. However, they tend to predict the region of the shock-wave oscillation slightly downstream. Interestingly, the WRILES can locate that region more

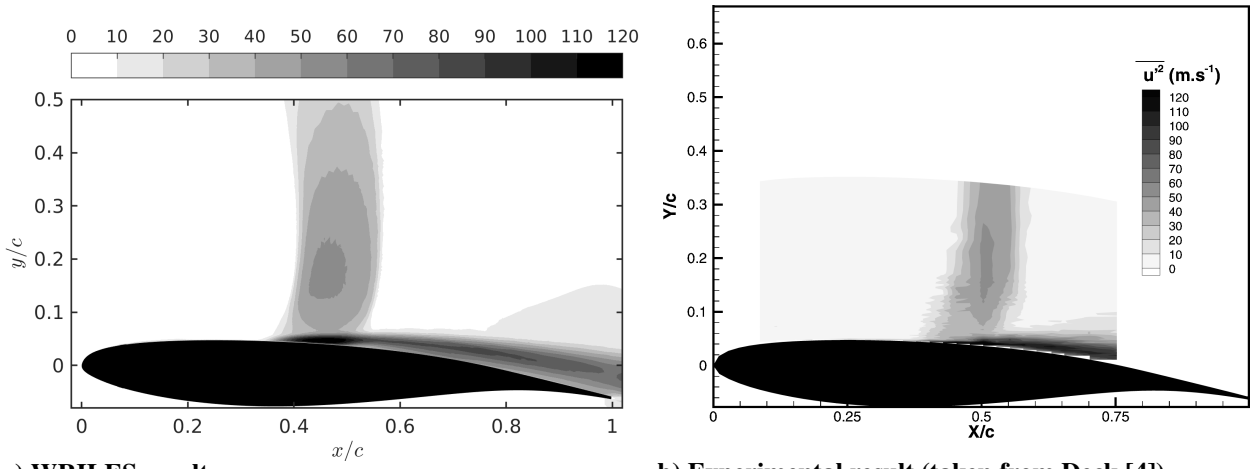

a) WRILES results **b) Experimental result (taken from Deck [4]).**

Fig. 4 Streamwise velocity fluctuations $\sqrt{\overline{u^{*\prime}u^{*\prime}}}$ over the airfoil obtained by WRILES and the corresponding experiments.

accurately, as illustrated by the peak of pressure fluctuations in the region of $0.35 \leq x/c \leq 0.55$, see Fig. 3. Moreover, the amplitude of pressure fluctuations agrees well with the experiment, and shows that the strength of the shock wave is also better predicted by the WRILES approach. The accurate prediction of the pressure fluctuations in the region of the attached TBL upstream of the shock indicates that the fluctuations of the inner-layer turbulence are resolved well enough with WRILES.

Fig. 4 shows the streamwise velocity fluctuations time-averaged over the 5 oscillations cycles and the experimental result [1]. We observe that the WRILES prediction matches well with the experimental result. Figures 6 and 7 show a good agreement for the velocity profiles computed downstream of the shock. However, very close to the wall in the attached TBL, the prediction is less accurate, probably because some features of the TBL are under-resolved.

Figure 5 shows the instantaneous Mach number distributions in the spanwise cross section and the isosurfaces of the Q-criterion colored by the streamwise velocity at two shock positions (most upstream position and most downstream position). The various scales of vortices are found over the airfoil in the oscillation cycle of the shock wave, and the WRILES resolves these vortex structures. At the boundary layer trip location $x/c = 0.07$, the expansion wave is generated due to the forced transition. Small-scale two-dimensional vortices are induced from the trip position and immediately break down to the fully developed turbulent boundary layers in the downstream. Typical hairpin-like vortices are found at the shock foot and they grow toward the downstream. When the shock wave is at the most downstream location, the shear layer is close to the wall, whereas when the shock wave is at the most upstream location, the separated shear layer is away from the wall. When the shock wave moves upstream, the shock wave becomes strong, and thus the large flow separation occurs. This large separation disappears when the shock wave starts to move downstream because the shock wave is weakened. These unsteady dynamics of the transonic airfoil buffet are also observed in the experiment [1] and in the WMLES simulation [6].

IV. Conclusion

In this paper, we perform a wall-resolved implicit large eddy simulation of transonic buffet phenomena over the OAT15A supercritical airfoil using the implicit local discontinuous Galerkin method. We develop a matrix-free Newton-GMRES method to solve the nonlinear systems arising from the DG discretization. This allows the DG solver to scale well on GPUs. In order to effectively resolve the boundary layers at high Reynolds numbers, we use a mesh refinement strategy to provide adequate resolution in the boundary layer region to capture flow transition and onset of turbulence. Without making use of either subgrid scale models or wall models, the WRILES method successfully predicts the buffet onset, the buffet frequency, and turbulence statistics. Various turbulence phenomena are predicted and demonstrated, such as periodic low-frequency oscillations of shock wave in the streamwise direction, strong shear layer-detached from the shock wave due to shock wave boundary layer interaction (SWBLI) and small scale structures

broken down by the shear layer instability in the transition region, and shock-induced flow separation. The pressure coefficient, the root mean square (RMS) of fluctuating pressure and streamwise range of shock wave oscillation agree well with experimental data.

Acknowledgments

The authors gratefully acknowledge NASA (under grant number NNX16AP15A) and the AFOSR (under grant number FA9550-16-1-0214) for supporting this work. Also, the authors thank the Barcelona Supercomputing Center which has provided access to its GPU cluster.

References

[1] Jacquin, L., Molton, P., Deck, S., Maury, B., and Soulevant, D., "Experimental study of shock oscillation over a transonic supercritical profile," *AIAA Journal*, Vol. 47, No. 9, 2009, pp. 1985–1994. doi:10.2514/1.30190, URL http://arc.aiaa.org/doi/10.2514/1.30190.

[2] Grossi, F., Braza, M., and Hoarau, Y., "Prediction of transonic buffet by delayed detached-eddy simulation," *AIAA Journal*, Vol. 52, No. 10, 2014, pp. 2300–2312. doi:10.2514/1.J052873, URL http://arc.aiaa.org/doi/10.2514/1.J052873.

[3] Thiery, M., and Coustols, E., "Numerical prediction of shock induced oscillations over a 2D airfoil: Influence of turbulence modelling and test section walls," *International Journal of Heat and Fluid Flow*, Vol. 27, No. 4, 2006, pp. 661–670. doi:10.1016/j.ijheatfluidflow.2006.02.013.

[4] Deck, S., "Numerical simulation of transonic buffet over a supercritical Airfoil," *AIAA Journal*, Vol. 43, No. 7, 2005, pp. 1556–1566. doi:10.2514/1.9885, URL http://arc.aiaa.org/doi/10.2514/1.9885.

[5] Huang, J., Xiao, Z., Liu, J., and Fu, S., "Numerical investigation of shock buffet on an OAT15A airfoil and control effects of vortex generators," *50th AIAA Aerospace Sciences Meeting*, 2012, pp. AIAA–2012–0044. doi:doi:10.2514/6.2012-44, URL https://doi.org/10.2514/6.2012-44.

[6] Fukushima, Y., and Kawai, S., "Wall-modeled large-eddy simulation of transonic airfoil buffet at high Reynolds number," *AIAA Journal*, Vol. 56, No. 6, 2018, pp. 2372–2388. doi:10.2514/1.J056537, URL https://arc.aiaa.org/doi/10.2514/1.J056537.

[7] Garnier, E., and Deck, S., "Large-eddy simulation of transonic buffet over a supercritical airfoil," Springer Berlin Heidelberg, Berlin, Heidelberg, 2010, pp. 135–141.

[8] Fernandez, P., Nguyen, N. C., and Peraire, J., "The hybridized discontinuous Galerkin method for implicit large-eddy simulation of transitional turbulent flows," *Journal of Computational Physics*, Vol. 336, 2017, pp. 308–329. doi:10.1016/j.jcp.2017.02.015.

[9] Spalart, P. R., "Strategies for turbulence modelling and simulations," *International Journal of Heat and Fluid Flow*, Vol. 21, Elsevier, 2000, pp. 252–263. doi:10.1016/S0142-727X(00)00007-2, URL https://www.sciencedirect.com/science/article/pii/S0142727X00000072.

[10] Beck, A. D., Bolemann, T., Flad, D., Frank, H., Gassner, G. J., Hindenlang, F., and Munz, C.-D., "High-order discontinuous Galerkin spectral element methods for transitional and turbulent flow simulations," *International Journal for Numerical Methods in Fluids*, Vol. 76, No. 8, 2014, pp. 522–548. doi:10.1002/fld.3943, URL http://doi.wiley.com/10.1002/fld.3943.

[11] Frere, A., Hillewaert, K., Chivaee, H. S., Mikkelsen, R. F., and Chatelain, P., "Cross-validation of mumerical and experimental studies of transitional airfoil performance," *33rd Wind Energy Symposium*, AIAA SciTech Forum, American Institute of Aeronautics and Astronautics, 2015. doi:doi:10.2514/6.2015-0499, URL https://doi.org/10.2514/6.2015-0499.

[12] Gassner, G. J., and Beck, A. D., "On the accuracy of high-order discretizations for underresolved turbulence simulations," *Theoretical and Computational Fluid Dynamics*, Vol. 27, 2013, pp. 221–237. doi:10.1007/s00162-011-0253-7.

[13] Murman, S. M., Diosady, L., Garai, A., and Ceze, M., "A space-time discontinuous-Galerkin approach for separated flows," *54th AIAA Aerospace Sciences Meeting*, 2016, pp. AIAA–2016–1059. doi:doi:10.2514/6.2016-1059, URL https://doi.org/10.2514/6.2016-1059.

[14] Renac, F., de la Llave Plata, M., Martin, E., Chapelier, J. B., and Couaillier, V., "Aghora: A high-order DG solver for turbulent flow simulations," Springer International Publishing, Cham, 2015, pp. 315–335. doi:10.1007/978-3-319-12886-3_15, URL https://doi.org/10.1007/978-3-319-12886-3{_}15.

[15] Uranga, A., Persson, P.-O., Drela, M., and Peraire, J., "Implicit large eddy simulation of transition to turbulence at low Reynolds numbers using a discontinuous Galerkin method," *International Journal for Numerical Methods in Engineering*, Vol. 87, No. 1-5, 2011, pp. 232–261. doi:10.1002/nme.3036, URL http://dx.doi.org/10.1002/nme.3036.

[16] de Wiart, C. C., and Hillewaert, K., "Development and validation of a massively parallel high-order solver for DNS and LES of industrial flows," Springer International Publishing, Cham, 2015, pp. 251–292. doi:10.1007/978-3-319-12886-3_13, URL https://doi.org/10.1007/978-3-319-12886-3{_}13.

[17] Pazner, W., Franco, M., and Persson, P.-O., "High-order wall-resolved large eddy simulation of transonic buffet on the OAT15A airfoil," *AIAA Scitech 2019 Forum*, AIAA SciTech Forum, American Institute of Aeronautics and Astronautics, 2019. doi:doi:10.2514/6.2019-1152, URL https://doi.org/10.2514/6.2019-1152.

[18] Fernandez, P., Nguyen, N. C., and Peraire, J., "A physics-based shock capturing method for unsteady laminar and turbulent flows," *56th AIAA Aerospace Sciences Meeting*, Orlando, Florida, 2018, pp. AIAA–2018–0062.

[19] Moro, D., Nguyen, N. C., and Peraire, J., "Dilation-based shock capturing for high-order methods," *International Journal for Numerical Methods in Fluids*, Vol. 82, No. 7, 2016, pp. 398–416. doi:10.1002/fld.4223.

[20] Nguyen, N. C., and Peraire, J., "Hybridizable discontinuous Galerkin methods for partial differential equations in continuum mechanics," *Journal of Computational Physics*, Vol. 231, No. 18, 2012, pp. 5955–5988. doi:10.1016/j.jcp.2012.02.033, URL http://linkinghub.elsevier.com/retrieve/pii/S0021999112001544.

[21] Cockburn, B., and Shu, C.-W., "The local discontinuous Galerkin method for time-dependent convection-diffusion systems," *SIAM Journal on Numerical Analysis*, Vol. 35, No. 6, 1998, pp. 2440–2463. doi:10.1137/S0036142997316712, URL http://epubs.siam.org/doi/abs/10.1137/S0036142997316712.

[22] Alexander, R., "Diagonally implicit Runge-Kutta methods for stiff ODEs," *SIAM J. Numer. Anal.*, Vol. 14, 1977, pp. 1006–1021.

[23] Marquardt, D. W., "An algorithm for least-squares estimation of nonlinear parameters," *SIAM*, Vol. 11, No. 2, 1963, pp. 431–441.

[24] Broyden, C. G., "The convergence of a class of double-rank minimization algorithms 1. General considerations," *IMA Journal of Applied Mathematics*, Vol. 6, No. 1, 1970, pp. 76–90. doi:10.1093/imamat/6.1.76, URL http://imamat.oxfordjournals.org/content/6/1/76.abstract.

[25] Fletcher, R., "A new approach to variable metric algorithms," *The Computer Journal*, Vol. 13, No. 3, 1970, pp. 317–322. doi:10.1093/comjnl/13.3.317, URL http://comjnl.oxfordjournals.org/content/13/3/317.short?rss=1{&}ssource=mfc.

[26] Goldfarb, D., "A family of variable-metric methods derived by variational means," *Mathematics of Computation*, Vol. 24, No. 109, 1970, pp. 23–23. doi:10.1090/S0025-5718-1970-0258249-6, URL http://www.ams.org/mcom/1970-24-109/S0025-5718-1970-0258249-6/.

[27] Shanno, D. F., "Conditioning of quasi-Newton methods for function minimization," *Mathematics of Computation*, Vol. 24, No. 111, 1970, pp. 647–647. doi:10.1090/S0025-5718-1970-0274029-X, URL http://www.ams.org/mcom/1970-24-111/S0025-5718-1970-0274029-X/.

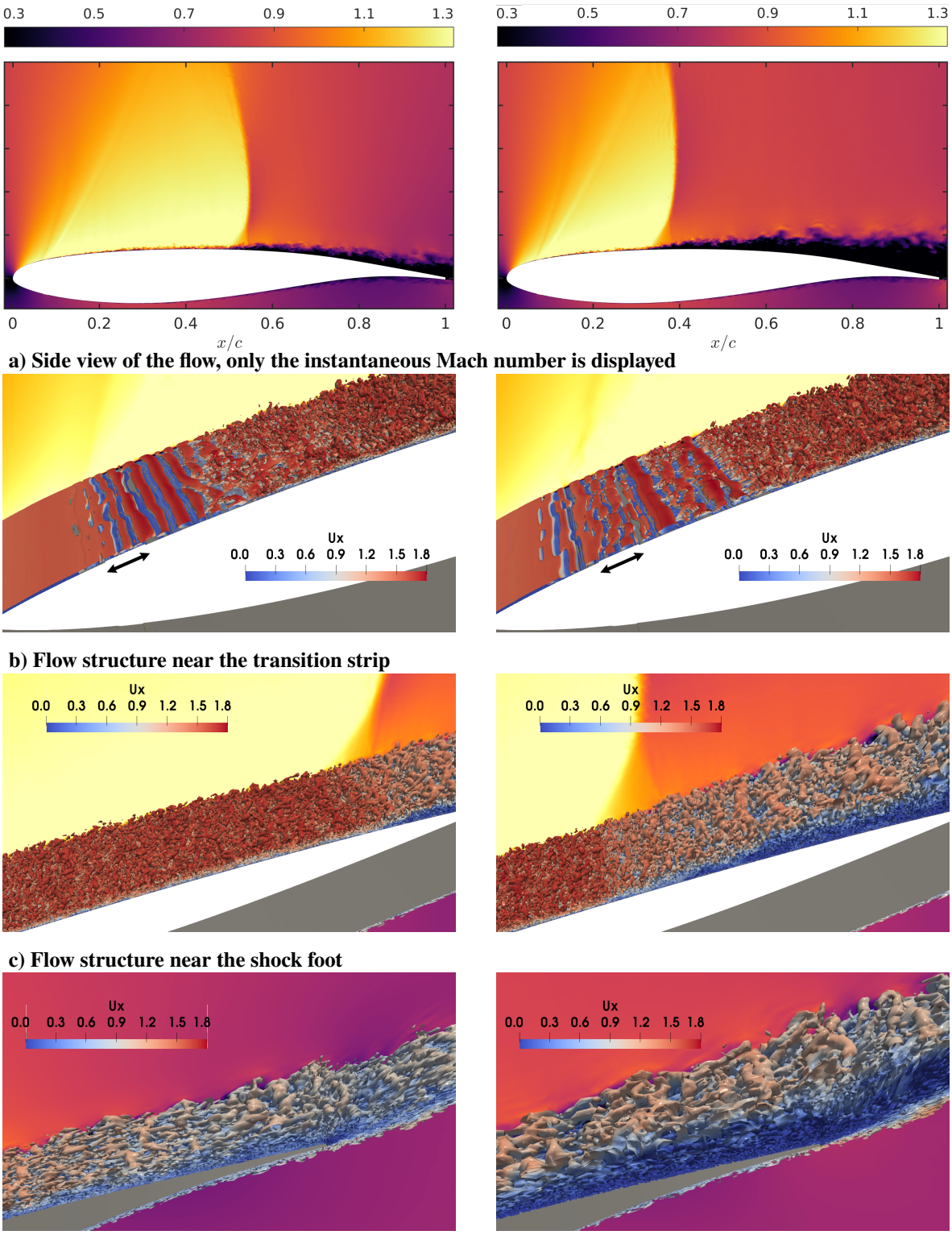

Fig. 5 Instantaneous Mach number at $z = 0$ and isosurfaces of Q-criterion ($Q/M_\infty^2 = 200$) colored by the streamwise velocity obtained by WRILES. Left column : maximal upstream shock location ($tu_\infty/c = t_0$). Right column: maximal downstream shock location ($t = t_0 + 0.5T_s$). On b), the strip width is indicated with an arrow.

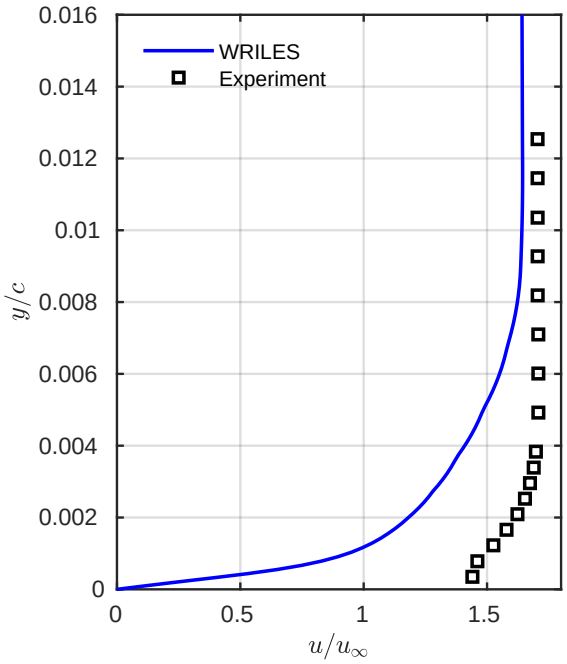

a) $x/c = 0.28$

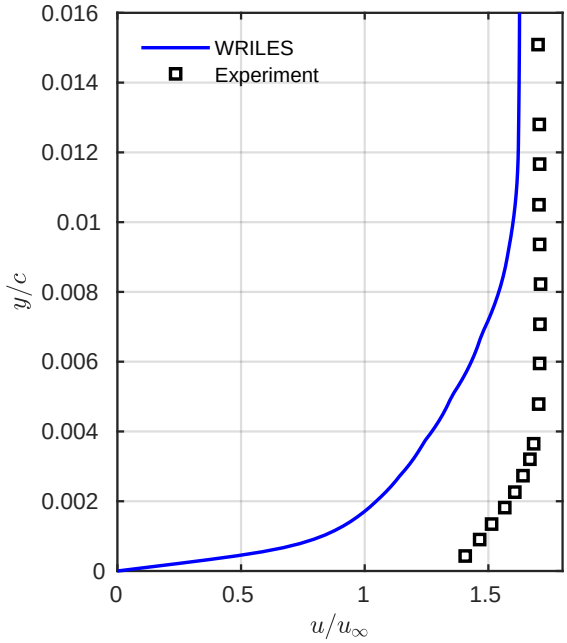

b) $x/c = 0.35$

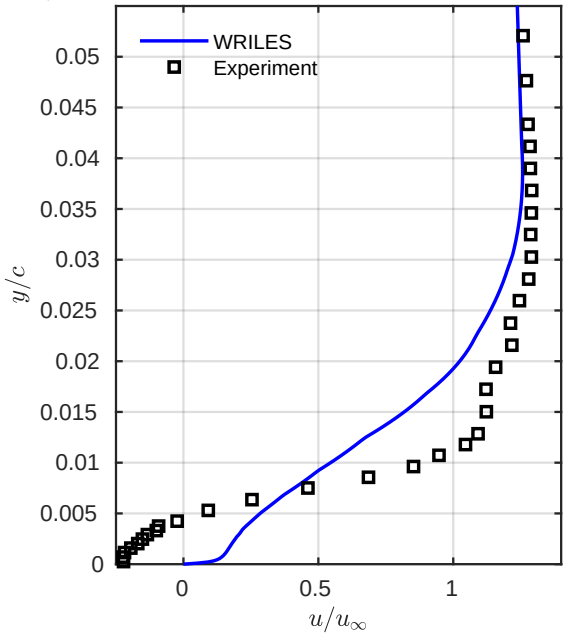

b) $x/c = 0.55$

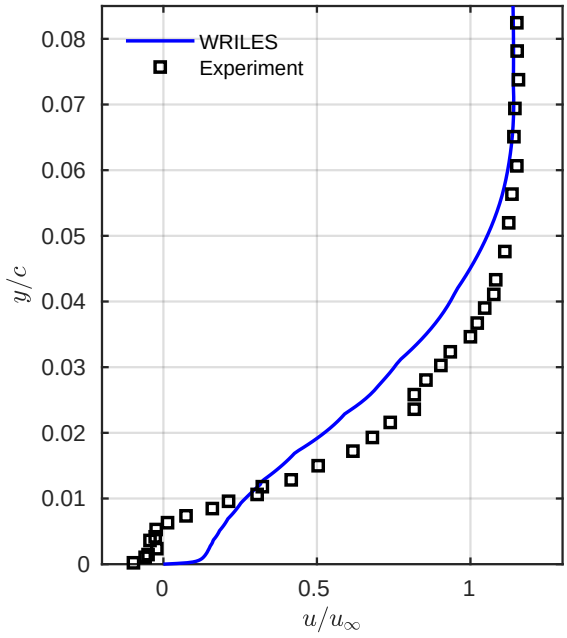

b) $x/c = 0.75$

Fig. 6 Spanwise-and-time-averaged streamwise velocity profiles on the suction surface compared with experimental data.

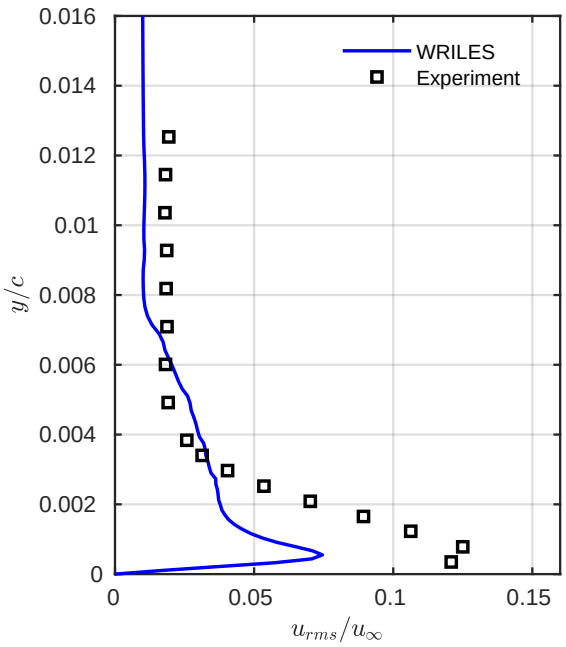

a) $x/c = 0.28$

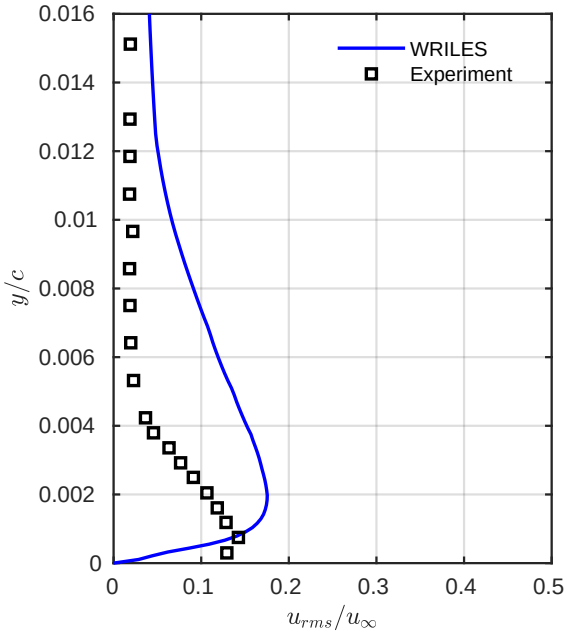

b) $x/c = 0.35$

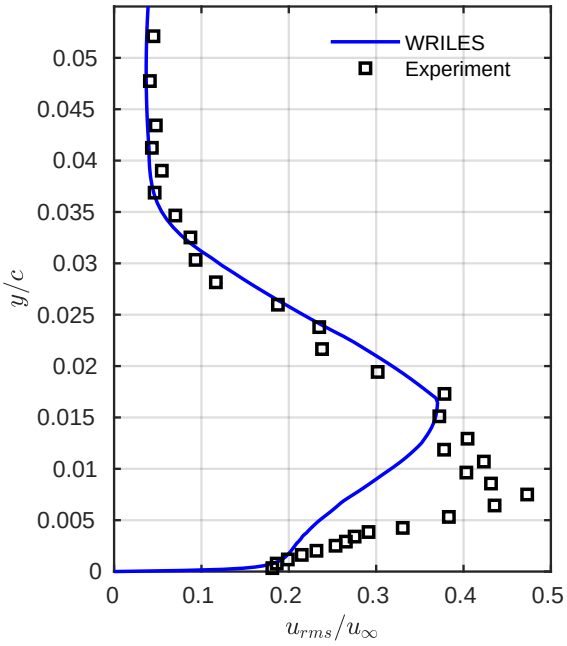

b) $x/c = 0.55$

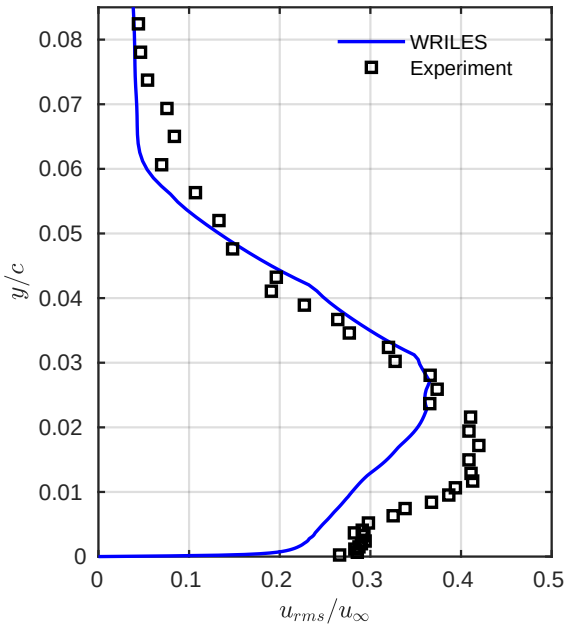

b) $x/c = 0.75$

Fig. 7 Standard deviations of the streamwise velocity profiles on the suction surface compared with experimental data.